Liquid Crystals
Publication details, including instructions for authors and subscription information:
http://www.informaworld.com/smpp/title~content=t713926090

Microstructure and thermodynamics of a lamellar phase with disrupted surfactant bilayers

P-O. Quest[a]; K. Fontell[ab]; B. Halle[a]
[a] Condensed Matter Magnetic Resonance Group, Chemical Center, Lund University, Lund, Sweden [b] Departments of Physical Chemistry,

To cite this Article Quest, P-O. , Fontell, K. and Halle, B.(1994) 'Microstructure and thermodynamics of a lamellar phase with disrupted surfactant bilayers', Liquid Crystals, 16: 2, 235 — 256
To link to this Article: DOI: 10.1080/02678299408029149
URL: http://dx.doi.org/10.1080/02678299408029149

LIQUID CRYSTALS, 1994, VOL. 16, NO. 2, 235–256

Microstructure and thermodynamics of a lamellar phase with disrupted surfactant bilayers

by P-O. QUIST*, K. FONTELL† and B. HALLE

Condensed Matter Magnetic Resonance Group, Chemical Center, Lund University, P.O.Box 124, S-221 00 Lund, Sweden

(*Received 2 June 1993; accepted 17 August 1993*)

Intrinsic structural defects in the lamellar (L_α) phase of the system sodium dodecyl sulphate (**SDS**)/decanol/water are studied by a combination of NMR ^2H quadrupole splittings of α-deuteriated **SDS** and small angle X-ray scattering (SAXS). The focus is on the variation of the density and size of the defects with the bilayer composition (decanol/**SDS** mol ratio 0·46–2·5), the bilayer volume fraction (0·27–0·64), and the temperature (20–40°C). It is found that bilayer defects are promoted by a small decanol/**SDS** ratio in the bilayers and by a low bilayer volume fraction, i.e. the same factors that drive the progression of phases towards microstructures with more highly curved interfaces. Variations of the extent of defects in the L_α phase reflect variations of the number of defects rather than changes of their size. The data are consistent with either slit defects (slit width ~ 10 Å) or pore defects (diameter ~ 25 Å). In either case, the interface separation across the defect is considerably smaller than the inter-bilayer separation. There is no evidence of transitions between L_α phases with different defect patterns. The defect variation with composition is analysed in terms of a simple thermodynamic model, showing that, apart from the electrostatic bilayer repulsion (which opposes defects), it is necessary to allow for considerable variations of the defect self-energy (which promotes defects).

1. Introduction

A rapidly growing number of studies [1–23] have demonstrated that the lamellar (L_α) phase in many binary and ternary amphiphile/water systems can have a microstructure that deviates from the classical stacking of planar homogeneous bilayers. Under certain conditions, it is found that the bilayers are extensively disrupted by slit-like or pore-like defects that introduce water in the bilayer core and impart a positive mean curvature to the surfactant monolayer. The study of these intrinsic structural defects in the L_α phase may give important contributions to the general understanding of microstructure and phase behaviour in lyotropic systems and may also have implications for lipid membranes in biological systems (permeability, fusion, protein incorporation).

Direct evidence for structural defects in L_α phases has come mainly from studies of diffusion [1–5] and conductivity [6–11] anisotropy, diffuse lateral scattering of X-rays and neutrons [12–22], and nuclear spin relaxation anisotropy [23]. However, defects are also manifested in the Bragg spacing (d), which decreases as water is transferred from the interlamellar space to the bilayer core, and in the NMR quadrupole splitting ν_Q, which decreases due to additional motional averaging over the curved defect surface.

* Author for correspondence.
† Departments of Physical Chemistry 1 and 2.

0267–8292/94 $10·00

The latter two quantities are routinely obtained from small angle X-ray scattering (SAXS) patterns and NMR lineshapes, respectively. To extract information about defects from d and ν_Q, however, one must know the bilayer thickness and the residual quadrupole coupling (or local order parameter), respectively. If these quantities are known, the SAXS data given directly the fraction of the bilayer volume occupied by defects, while the NMR data yield, for a given defect geometry, the relative dimensions of the defects.

In a recent study of the counterion ^{23}Na spin relaxation anisotropy from a sample in the L_α phase of the system sodium dodecyl sulphate (**SDS**)/decanol/water, we established the existence of a high density of slit or pore defects [23]. In the present work we study how the density and size of the defects vary with composition and temperature, with the aim of gaining an understanding of the driving force for defect formation. Since we wanted to study a larger number of sample compositions and temperatures, we measured Bragg spacings (SAXS) and ^{2}H quadrupole splittings of α-deuteriated **SDS** rather than the time consuming spin relaxation anisotropy.

In § 3 we determine the defect volume fraction Ψ from the SAXS data: Ψ increases dramatically as the decanol/**SDS** ratio is reduced, and decreases gradually as the bilayer separation is reduced. By combining the SAXS and NMR data and assuming either a slit or a pore geometry for the defects, we then show that the defect size (slit width or pore diameter) remains essentially constant as Ψ varies.

In § 4 we investigate the thermodynamic implications of the composition dependence of the defect density established in § 3. We do this within the simple semi-phenomenological framework proposed by Bagdassarian *et al.* [24], where defects are promoted by a self-energy per defect and opposed by the electrostatic inter-bilayer repulsion. The disappearance of defects with decreasing bilayer separation is found to be more gradual then expected for a constant defect self-energy. The strong increase in defect density with decreasing decanol/**SDS** ratio is dominated by changes in the self-energy, reflecting an increasing spontaneous curvature. Temperature variations within a 20°C interval were found to have a barely significant effect on the defect density.

2. Experimental

2.1. *Materials and sample preparation*

The samples were made from a mixture of **SDS** (sodium dodecyl sulphate, specially pure, from Merck Ltd, U.K.) and α-deuteriated **SDS** (from Synthelec, Lund, purified by repeated recrystallization from aqueous solution), decanol (1-decanol, specially pure, from Merck Ltd, U.K.), and millipore filtered H_2O.

The samples were prepared by weighing protonated and α-deuteriated **SDS** (mol fraction *c.* 1 : 1), decanol and water into 7·5 mm i.d. Pyrex glass tubes, which immediately were flame-sealed. The samples were vigorously mixed several times during the first week and then allowed to equilibrate at 25°C during 3 weeks before any measurements were performed.

The sample compositions are shown in the ternary phase diagram in figure 1, and the molar compositions are listed in table 1. The samples fall on three lines in the phase diagram: the **Wa** and **Wb** lines, which have a constant bilayer composition ($y \equiv n_{dec}/n_{SDS} \approx 1{\cdot}06$ and 0·48, respectively) and varying water content, and the **D** line, where we add decanol to the bilayer keeping the H_2O/**SDS** molar ratio constant at $x \equiv n_w/n_{SDS} \approx 38{\cdot}2$. Since the three lines intersect at two compositions, two pairs of samples are identical: **D1** = **Wb2** and **Wa2** = **D5**.

2.2. *NMR experiments*

The ^2H NMR experiments were performed using three spectrometers: a Bruker MSL-100, a Varian Unity 300, and a Nicolet Nic-360 equipped with vertical saddle-coil probes and 2·35, 7·05, and 8·5 T superconducting magnets. The 90° pulse duration was approximately 10, 25, and 20 μs. The pulses were applied on resonance (at the centre of the spectrum).

The temperature was controlled by airflow temperature regulators, yielding a temperature stability of $\pm 0{\cdot}2$°C or better. Unless otherwise stated, the reported quadrupole splittings were obtained at 25·0°C.

The ^2H spectra were accumulated with the quadrupolar echo sequence $(\pi/2)_x - \tau - (\pi/2)_{\pm y} - \tau -$ acq., with the delay time $\tau \approx 50$ μs. Typically, the spectral width was set to 100 kHz. Prior to Fourier transformation, the FIDs were zero-filled to an appropriate level.

Figure 2 shows the ^2H spectrum of α-**SDS** in sample **D1** obtained on the Nicolet at 25°C. The effective uniaxial symmetry (which was present in all investigated samples) of the L_α phase is evident from the powder lineshape. The quadrupole powder splitting, ν_Q, measured as the peak-to-peak separation in the spectrum, is given for all samples in table 1 and in figures 3–5.

2.3. *SAXS experiments*

The small angle X-ray scattering (SAXS) experiments were performed at 25°C. The Bragg reflections were recorded in duplicate directly on film in a Kiessig camera, using pin-hole collimation and monochromatic (Ni filtered) CuK_α radiation ($\lambda = 1{\cdot}54$ Å). The

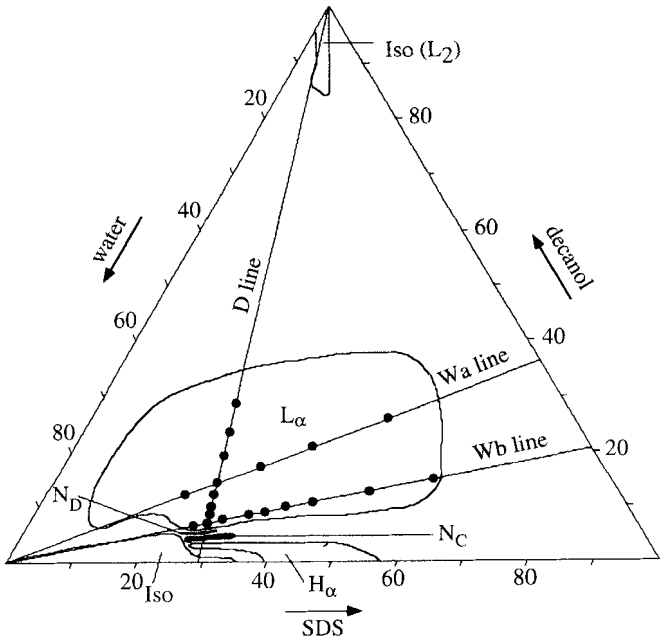

Figure 1. Partial phase diagram (wt per cent) for the system **SDS**/decanol/water (90 per cent $H_2O + 10$ per cent D_2O) at 25°C showing the extension of the one phase regions of the lamellar (L_α), hexagonal (H_α), and nematic (N_C, N_D) liquid crystalline phases and the isotropic micellar solution phase (Iso). The dots along the three lines correspond to the investigated samples.

Table 1. Sample compositions, ^2H quadrupole splitting ν_Q, and lamellar period d.

Sample	x†	y†	ϕ‡	ν_Q/kHz§	d/Å¶
D1	38·0	0·480	0·288	17·2	58·6
D2	38·2	0·600	0·301	20·8	64·6
D3	38·2	0·700	0·313	23·9	70·0
D4	38·2	0·870	0·332	24·6	—
D5	38·2	1·06	0·352	24·8	64·6
D6	38·2	1·50	0·392	24·8	55·3
D7	38·2	1·96	0·429	24·8	54·3
D8	38·2	2·54	0·469	24·6	—
Wa1	49·2	1·07	0·301	24·4	77·4
Wa2	38·2	1·06	0·352	24·8	64·6
Wa3	27·7	1·06	0·424	24·8	56·1
Wa4	18·4	1·06	0·516	25·1	45·1
Wa5	9·9	1·06	0·644	26·0	38·7
Wb1	42·2	0·458	0·266	15·6	64·3
Wb2	38·0	0·480	0·288	17·2	58·6
Wb3	34·3	0·496	0·311	18·2	59·4
Wb4	28·0	0·475	0·350	18·6	53·6
Wb5	25·2	0·475	0·373	19·2	51·4
Wb6	21·8	0·493	0·407	20·5	51·4
Wb7	18·1	0·480	0·446	20·8	44·2
Wb8	12·1	0·487	0·535	23·2	41·5
Wb9	7·3	0·469	0·633	26·2	36·5

† x = mol H_2O/mol **SDS**, y = mol decanol/mol **SDS**.

‡ ϕ = volume fraction hydrocarbon chains in sample, calculated using the group volumes given in [23].

§ Uncertainty: ±0·2 kHz.

¶ Uncertainty: ±5 per cent.

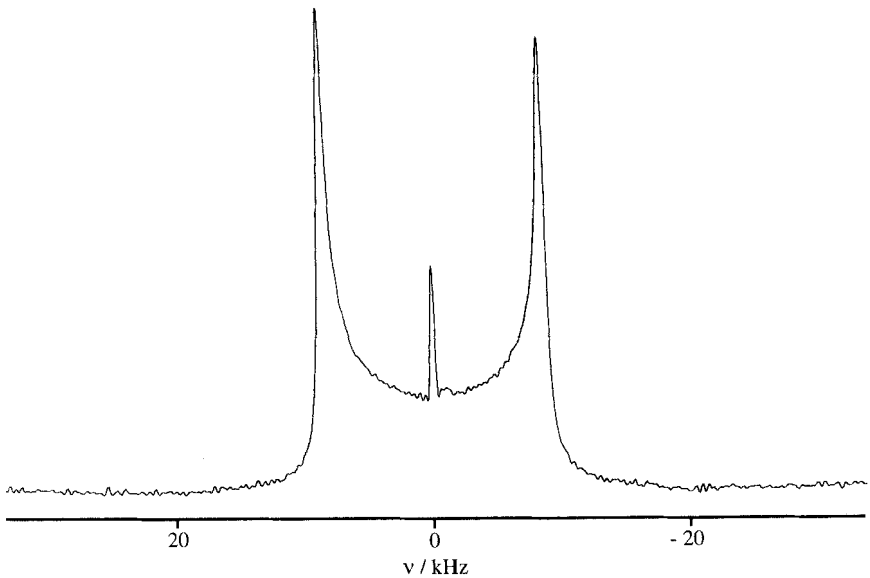

Figure 2. ^2H NMR spectrum of sample **D1** at 25°C. The small peak at the centre is the (distorted due to FID truncation) contribution from water deuterons.

SAXS samples were prepared from the NMR samples in the following way: the flame-sealed Pyrex tube was cut and a small fraction of the sample was transferred to a Lindemann capillary, which immediately was flame-sealed and placed into the X-ray diffractometer.

The SAXS patterns revealed the first and frequently the second Bragg reflection. When two reflections were detected, their relative positions agreed with the theoretical prediction (1 : 1/2) for a lamellar phase. The lamellar period, d, obtained from the Bragg spacings is given for all investigated samples in table 1 and in figures 3–5.

3. Microstructure

3.1. *Bilayer thinning versus defect formation*

Figures 3–5 show the evolution along the **D**, **Wa**, and **Wb** lines of the quadrupole splitting ν_Q, obtained from the α-SDS ^{2}H NMR lineshape, and the apparent bilayer thickness, which can be expressed as a product of ϕ and d, obtained from the SAXS pattern. Along each of the three lines, ν_Q and ϕd vary in a similar way.

With increasing decanol/**SDS** ratio (**D** line), ν_Q and ϕd first increase rapidly and then abruptly level off at limiting values of *c.* 25 kHz and 23 Å, respectively. Figure 3 includes also the SAXS data of Hendrikx *et al.* [16], from the L_α phase in the **SdS**/decanol/water system (**SdS** = sodium decyl sulphate). In both systems, the break-point occurs at a decanol/surfactant ratio of $y \approx 0{\cdot}8$.

As the water content is reduced at a fixed decanol/**SDS** ratio above the break-point (i.e. on the plateau in figure 3), both ν_Q and ϕd remain nearly constant at their limiting values (see figure 4). However, when the water content is reduced at a decanol/**SDS** ratio well below the break-point, both ν_Q and ϕd increase gradually and reach their limiting values only at the lowest water content (see figure 5). The scatter of the data on the **Wb** line (figure 5) is partly due to slight variations in the decanol/**SDS** ratio (cf. table 1 and figure 3).

Provided that (the alkyl chains of) all amphiphilic molecules (**SDS** and decanol) are confined to lamellar regions of thickness $2b$, the measured apparent bilayer thickness ϕd can be expressed as

$$\phi d = 2b(1 - \Psi), \tag{3.1}$$

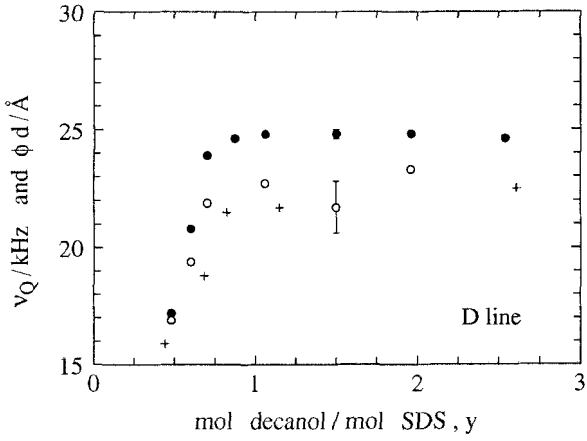

Figure 3. Variation of the quadrupole splitting, ν_Q, (●) and the apparent bilayer thickness, ϕd, (○), with the decanol/**SDS** ratio along the **D** line. We also include ϕd data (+) for the **SdS**/decanol/water system, previously reported by Hendrikx *et al.* [16].

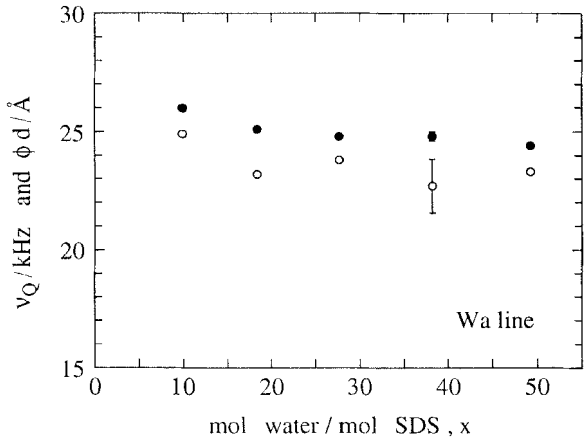

Figure 4. Variation of the quadrupole splitting, ν_Q, (●) and the apparent bilayer thickness, ϕd, (○), with the water/**SDS** ratio along the **Wa** line.

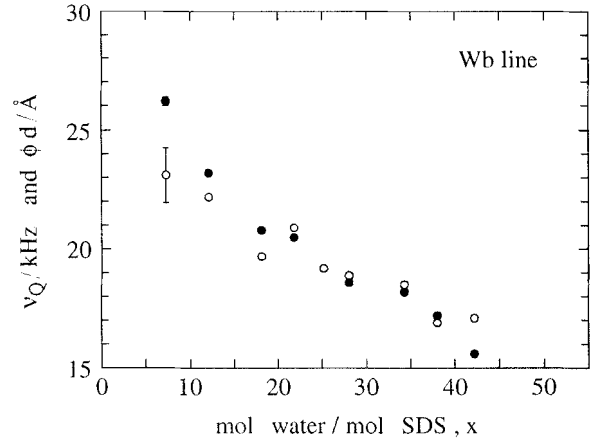

Figure 5. Variation of the quadrupole splitting, ν_Q, (●) and the apparent bilayer thickness, ϕd, (○), with the water/**SDS** ratio along the **Wb** line.

with Ψ the volume fraction of polar material (water, ions, and head groups) within the nonpolar bilayer core (of thickness $2b$).

The ^{2}H quadrupole splitting ν_Q from a powder sample of a uniaxial phase is given by

$$\nu_Q = \tfrac{3}{4}\alpha\bar{\chi}, \tag{3.2}$$

where $\bar{\chi}$ is the residual (locally averaged) quadrupole coupling constant and α is a shape factor. When the quadrupole coupling is of intramolecular origin, as in the present case, one usually makes the further decomposition $\bar{\chi} = S\chi$, where χ refers to a molecule-fixed principal frame for the quadrupole coupling ($\chi \approx 170$ kHz for aliphatic deuterons) and S is the (second rank) orientational order parameter for the principal axis (the C_α–^{2}H bond in the present case) with respect to the interface normal. Typically, C_α–^{2}H bonds in L_α phases have $S \approx 0{\cdot}2$ for alkyl sulphates and $S \approx 0{\cdot}3$ for alkanoates. The shape factor α depends on the shape of the hydrocarbon–water interface and on the lateral distribution of the spin-bearing species over that interface (cf. § 3.2).

The water ^2H and counterion ^{23}Na quadrupole splittings also contain information about the shape of the interface. However, in these cases the residual quadrupole coupling constant $\bar{\chi}$ depends more strongly on the sample composition. While $\bar{\chi}$ can be determined from the spin relaxation anisotropy [23], we consider here only α-**SDS** ^2H splittings, where $\bar{\chi}$ varies only weakly with composition (cf. below).

According to equation (3.1), the observed reduction of ϕd (with increasing x or decreasing y) from its limiting value of *c.* 23 Å can have two different causes: bilayer thinning (decreasing b) or defect formation (increasing Ψ). Although both effects can be expected *a priori*, we shall argue that defect formation is the dominant cause. The argument is based on the following three observations.

First, *direct* experimental evidence for bilayer defects, with Ψ values close to those predicted by equation (3.1) with constant b, is provided (i) by the strong anisotropy in the ^{23}Na spin relaxation from an aligned sample of the present L_α phase [23] (at the same composition as sample D1), and (ii) by the lateral (diffuse) scattering in the SAXS pattern from aligned samples (with $y<0{\cdot}8$) of the L_α phase in the **SdS**/decanol/water system [16]. Thinning of a classical (planar and homogeneous) bilayer would produce neither relaxation anisotropy nor lateral scattering.

The second argument against bilayer thinning is based on a thermodynamic analysis presented in the Appendix. For a classical L_α phase (without defects) at a given fixed composition (x, y), the bilayer thickness is essentially determined by the balance between the electrostatic free energy, which tends to make the bilayer thinner, since this reduces the surface charge density, and the (effective) interfacial free energy, which favours a thick bilayer with a smaller interface area [25]. In addition to these forces, the strong short-ranged lateral repulsion between the surfactant head groups establishes a minimum head group area (at the interface) and, hence, a maximum bilayer thickness ($2b_{max}$). This maximum bilayer (core) thickness is simply given by ϕd above the breakpoint on the **D** line and on the entire **Wa** line, where there should be no defects. From the data in figures 3 and 4 we thus obtain $b_{max} = 11{\cdot}6$ Å. According to the analysis in the Appendix, all the 'equilibrium' b values, resulting from balance between electrostatic push and interfacial pull, exceed b_{max}. Hence, for all the investigated samples, the bilayer has its maximum thickness, i.e. $b = b_{max}$.

The third argument against bilayer thinning comes from an analysis of the quadrupole splittings. Although bilayer thinning should lead to a reduction of ν_Q (as observed), since the order parameter S decreases with increased head group area, the observed 40 per cent reduction of ν_Q is at least an order of magnitude larger than the expected reduction of S [26]. (For the C–^2H bonds further down the alkyl chain, S is more sensitive to the headgroup area.)

Even for a bilayer of constant thickness (and, hence, constant head group area), S (and, thus, $\bar{\chi}$) may depend on composition (x and y). However, previously reported ^2H quadrupole splittings for the α-position of the surfactant in a variety of systems [26–28] demonstrate that the composition dependence of S is an order of magnitude smaller than the ν_Q variations shown in figures 3 and 5. For example, in the sodium caprylate/decanol/water system, S decreases from 0·27–0·26 in the hexagonal (H_α) phase ($y = 0$–$0{\cdot}23$, $x = 9{\cdot}3$) and increases from 0·28 to 0·29 in the L_α phase ($y = 1{\cdot}0$–$1{\cdot}6$, $x = 9{\cdot}3$) [27]. (Again, the dependence is stronger for positions further down the alkyl chain.) Consequently, we take $\bar{\chi}$ to be independent of y along the **D** line. From the plateau region in figure 3, we obtain $\bar{\chi} = 33{\cdot}0$ kHz. The order parameter S is generally found to decrease with increasing water content (x) [27, 28]; strongly at low water content ($x < 10$) [28] and more weakly at high water content [27]. From the ν_Q data on

the **Wa** line see (figure 4), where there should be no defects, we obtain a weak linear x dependence according to $\bar{\chi}/\text{kHz} = 34{\cdot}7 - 0{\cdot}0464x$. Since $\bar{\chi}$ is insensitive to the decanol content (cf. above), we assume that this (weak) x dependence applies also to the **Wb** line (where $y \approx 0{\cdot}48$, as compared to $y = 1{\cdot}06$ on the **Wa** line).

3.2. *Density and geometry of defects.*

The variation of the defect volume fraction Ψ along the **D** and **Wb** lines can be obtained from equation (3.1), the measured apparent bilayer thickness ϕd (see figures 3 and 5), and the constant bilayer half-thickness $b = 11{\cdot}6$ Å (cf. § 3.1). The resulting Ψ values are given in table 2. While these results are essentially model-independent, they do not provide direct information about the microstructure. In particular, the SAXS data do not tell us whether Ψ variations reflect changes in defect density (number of defects per unit area in the bilayer plane), or changes in defect size (aqueous intra-bilayer volume per defect), or a combination of the two. Furthermore, nothing can be inferred about the shape of the defects.

The quadrupole splitting ν_Q contains information about microstructure through the shape factor α. Using (3.2) and the $\bar{\chi}$ values established in § 3.1, we obtain the α values given in table 2. If θ is the angle between the symmetry axis of the uniaxial phase (the normal to the bilayer planes in the L_α phase) and the (assumed uniaxial) local interface normal, then

$$\alpha = 1 - \tfrac{3}{2}\langle \sin^2 \theta \rangle, \tag{3.3}$$

where the average is over the interfacial distribution of the spin-bearing species (**SDS**). If the bilayer consists of regions with planar and curved interfaces, the shape factor α appearing in equation (3.2) becomes

$$\alpha = (1 - P)\alpha_P + P\rho\alpha_C = 1 - P(1 - \rho\alpha_C), \tag{3.4}$$

Table 2. Defect volume fraction Ψ and defect propensity K, derived from SAXS data, and shape factor α, derived from NMR data, for samples with $\Psi \neq 0$.

Sample	Ψ†	K	α‡
D1	0·27	1·7 ± 0·2	0·70
D2	0·16	1·4 ± 0·1	0·84
D3	0·06	1·2 ± 0·1	0·97
Wb1	0·26	1·4 ± 0·1	0·64
Wb2	0·27	1·7 ± 0·2	0·70
Wb3	0·20	1·7 ± 0·2	0·73
Wb4	0·19	2·1 ± 0·2	0·74
Wb5	0·17	2·3 ± 0·3	0·76
Wb6	0·10	2·3 ± 0·3	0·81
Wb7	0·15	3·4 ± 0·5	0·82
Wb8	0·04	4·1 ± 0·6	0·91
SdS1§	0·28	5·1 ± 0·9	—
SdS2§	0·14	3·3 ± 0·5	—
SdS3§	0·02	2·5 ± 0·3	—

† Propagated uncertainty: ±0·04.

‡ Propagated uncertainty: ±0·01.

§ From SAXS data obtained by Hendrikx *et al.* [16], on the system **SdS**/decanol/D_2O at 23°C. Ψ calculated with $b = 11{\cdot}0$ Å (cf. figure 3).

with P the fraction of the **SDS** molecules that reside in curved regions. In equation (3.4) we allow the quadrupole coupling constant to vary between planar and curved regions, i.e., $\rho \equiv \bar{\chi}_C/\bar{\chi}_P \neq 1$. Since the interface curvature increases the headgroup area, we expect $\rho < 1$. For a sample ($x = 43{\cdot}1$, $y = 0{\cdot}245$) in the hexagonal (H_α) phase of the present system, we previously [29] obtained $\bar{\chi} = 29{\cdot}6$–$31{\cdot}5$ kHz at 25°C. Taking $\rho \approx \bar{\chi}(H_\alpha)/\bar{\chi}$(defect-free L_α), we thus have $\rho = 0{\cdot}90$–$0{\cdot}96$. For the C_α–^2H bond in other surfactants, $\bar{\chi}(H_\alpha)/\bar{\chi}(L_\alpha)$ is typically in the range 0·8–1·0 [26, 27, 30, 31]. In the following calculations we take $\rho = 0{\cdot}9$, although the change in the calculated geometric parameters due to this slight variation of the quadrupole coupling constant is barely significant.

Unlike the SAXS data, the quadrupole splittings cannot be interpreted without invoking a geometric model of the microstructure. The hydrocarbon/water topology within the bilayer can be either hydrocarbon-continuous, water-continuous, or bicontinuous. The corresponding microstructures may be thought of, respectively, as bilayers perforated by aqueous pores, discrete discoidal micelles positionally ordered on to planes, and bilayers cut by aqueous slits. In our recent ^{23}Na spin relaxation study of sample **D1**, we found that both pores and slits were consistent with the data (for certain relative dimensions), while discoids were not [23]. Since the water-continuous microstructure is thus experimentally ruled out at low volume fraction ($\phi = 0{\cdot}288$ in sample **D1**) and since it becomes impossible (due to inefficient packing) at high ϕ, we consider only the pore and slit geometries in the following.

Figure 6 illustrates the specific defect geometries considered: the hemitoroidal pore and the cylindrical slit/ribbon. The shape factor α_C for the curved region is

$$\alpha_C^{\text{pore}} = \frac{1}{4}\left(1 - \frac{2}{\pi\zeta}\right)^{-1}, \tag{3.5 a}$$

$$\alpha_C^{\text{slit}} = \tfrac{1}{4}, \tag{3.5 b}$$

with $\zeta = 1 + c_w/b$ (cf. figure 6). Apart from the different topology, there are two qualitative differences between the pore and slit (or ribbon) geometries. First, in contrast to the ribbon, the pore has a non-uniform curvature, which, moveover, depends on the defect size (c_w). As the pore radius $c_w \to \infty$, the hemitoroidal edge degenerates into a hemicylinder, i.e. $\alpha_C^{\text{pore}} = \alpha_C^{\text{slit}}$. Second, whereas the pore is uniaxial, the ribbon is of lower (D_{2h}) symmetry than the L_α phase ($D_{\infty h}$). To be consistent with the observed uniaxial powder pattern, the ribbons (and slits) must have an orientational distribution in the bilayer plane with at least threefold symmetry with respect to

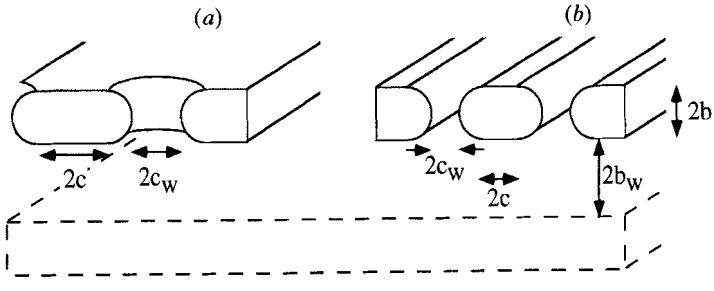

Figure 6. Cross-sections of the hemitoroidal pore (*a*) and cylindrical slit (*b*) defects with the geometric parameters defined. The shaded regions correspond to the cross-section of the hydrocarbon core of the bilayer.

the bilayer normal. The implies a non-zero curvature along the ribbon axis, but we assume that this curvature is sufficiently small for equation (3.5 *b*) to be an accurate approximation [cf. equation (3.5 *a*) with $c_w \gg b$].

The pore and slit microstructures may be regarded as convenient limiting geometries. The real microstructure may, of course, be intermediate between these limits (elongated pores, finite slits, or finite ribbons) and, moreover, may exhibit structural polydispersity (particularly at small Ψ).

The fraction P, appearing in equation (3.4), can be expressed as

$$P = \sigma \frac{V_C}{V_C + V_P}, \tag{3.6}$$

where V_C and V_P are the volumes of the curved and planar hydrocarbon regions and σ is a segregation factor. If the bilayer composition, which we measure by the decanol/**SDS** mol ratio y, is the same in the curved and planar regions, then $\sigma = 1$. In general,

$$\sigma = \frac{v_{SDS} + y v_{dec}}{v_{SDS} + y_C v_{dec}}, \tag{3.7}$$

with $v_{SDS} = 350\,\text{Å}^3$ and $v_{dec} = 296\,\text{Å}^3$ the respective alkyl chain volumes. Considering only electrostatic interactions, the charged **SDS** molecules should favour the curved regions ($y_C < y$) [32]. This effect has indeed been observed (but not yet quantified) in the rectangular (ribbon) phase in the system **SdS**/decanol/water [33]. In the present system, the different chain lengths of the two amphiphiles should reduce segregation somewhat, but we still expect more **SDS** in the curved regions. We thus expect that $1 \leqslant \sigma \leqslant \sigma_{max}$, with $\sigma_{max} = 1 + 0{\cdot}85y$ corresponding to a curved edge with no decanol at all.

For the ribbon, the volumes V_C and V_P depend on the bilayer thickness and on the ribbon width,

$$P = \frac{\sigma}{1 + 4\eta/\pi}, \tag{3.8}$$

with $\eta = c/b$ (cf. figure 6). The defect volume fraction depends also on the slit width ($2c_w$).

$$\Psi = \frac{\zeta - \pi/4}{\zeta + \eta}. \tag{3.9}$$

For the pore, the volumes V_C and V_P, like Ψ, depend on *both* η and ζ,

$$P = \sigma \frac{(\pi/2)\zeta - \frac{2}{3}}{[(\pi/2) + 2\eta]\zeta + \eta^2 - \frac{2}{3}}, \tag{3.10}$$

$$\Psi = \frac{\zeta[\zeta - (\pi/2)] + \frac{2}{3}}{(\zeta + \eta)^2}. \tag{3.11}$$

Eliminating η from equation (3.10), we obtain

$$P = \sigma \frac{\Psi}{1 - \Psi}\left(\frac{\zeta^2}{(\pi/2)\zeta - \frac{2}{3}} - 1\right)^{-1}. \tag{3.12}$$

For the slit/ribbon geometry, we can calculate η, and hence the ribbon width $2b + 2c$ from equations (3.4), (3.5 *b*), and (3.8), and the α values in table 2. Inserting these η values and the Ψ values (from the SAXS data) in table 2 into equation (3.9), we then obtain ζ,

and hence the slit width $2c_w$. The results (for $\rho = 0{\cdot}9$ and $\sigma = 1$) are collected in table 3 along with the thickness, $2b_w = d - 2b$, of the aqueous interbilayer region. The effect of quadrupole coupling variation ($\rho = 0{\cdot}9$ rather than $\rho = 1$) is in all cases within the propagated experimental error given in table 3. If we allow for segregation ($\sigma > 1$), the ribbon width and slit width increase by at most (for $\sigma = \sigma_{max} \approx 1{\cdot}41$) *c.* 35 per cent and 60 per cent, respectively. However, σ is probably closer to 1 than to σ_{max}.

The results in table 3 tell us two things. First, the increase of the defect volume fraction Ψ is due to a narrowing of the ribbons rather than a widening of the slits. At the highest Ψ values (samples **D1** and **Wb1**), the aspect ratio $(2b + 2c)/(2b)$ of the ribbons is *c.* 2. As expected, this is larger than the values of *c.* 1·3–1·9 reported for ribbon aggregates in rectangular phases [34]. Second, the nearly constant slit width is, in all cases, considerably smaller (by a factor 2–4) than the thickness of the interlamellar aqueous region. These geometric inferences are illustrated in figure 7 (left panels), showing cross-sections of the slit/ribbon microstructure for two samples on the D line.

For the pore geometry, we use equations (3.4), (3.5 *a*), and (3.12) with the α and Ψ values in table 2 to calculate ζ and, hence, the pore diameter $2c_w$. We then use equation (3.11) to obtain η and, hence, the pore separation $2b + 2c$. (We define a cell diameter $2c_w + 2b + 2c$ without reference to the in-plane pore distribution.) The results (for $\rho = 0{\cdot}9$ and $\sigma = 1$) are given in table 4 and in figure 7 (right panels), where we illustrate the formation of (pore) defects along the **D** line by two top-views. With $\sigma = \sigma_{max}$, $2b + 2c$ increase by *c.* 35 per cent and $2c_w$ by *c.* 50 per cent. The conclusions are qualitatively the same as for the slit geometry, albeit not so clear-cut. With a pore diameter of 25 Å, the average mean curvature $\langle H \rangle$ of the pore edge is only 4 per cent lower than the $c_w \to \infty$ (slit) limit of $1/(2b)$.

4. Thermodynamics

4.1. *Optimal defect density*

The defect volume fraction Ψ, and its variation with composition and temperature within the L_α phase, reflect the free energy change as defects are introduced in the bilayers under different conditions. To extract information about the thermodynamics of defect formation, we construct a variational free energy $G(\Psi)$ and identify the equilibrium defect volume fraction with that value of Ψ which minimizes $G(\Psi)$. We

Table 3. Geometric parameters, for samples with $\Psi \neq 0$, derived from the NMR and SAXS data assuming slit defects.

Sample	Ribbon width $(2b + 2c)$/Å	Slit width $2c_w$/Å	Aqueous layer thickness $2b_w$/Å
D1	51±1	12±3	35±3
D2	93±4	12±5	41±3
D3	416±97	19±23	47±4
Wb1	44±1	9±3	41±3
Wb2	51±1	12±3	35±3
Wb3	58±2	9±3	36±3
Wb4	60±2	8±3	30±3
Wb5	65±2	8±4	28±3
Wb6	80±3	3±4	28±3
Wb7	83±3	9±5	21±2
Wb8	155±13	2±8	18±2

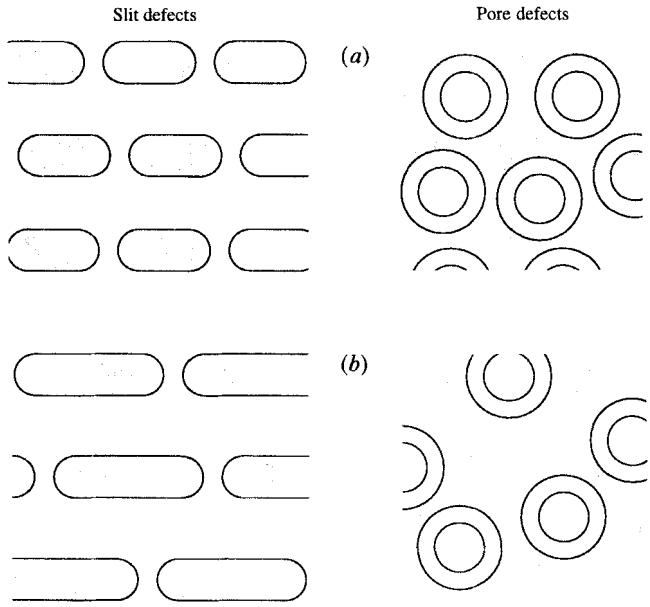

Figure 7. Cross-sections of bilayers with slit defects (left panels) and top views of bilayers with pore defects (right panels) corresponding to samples with different decanol/**SDS** ratio: (*a*) sample **D1** ($y=0{\cdot}48$, $\Psi=0{\cdot}27$), *b*) sample **D2** ($y=0{\cdot}60$, $\Psi=0{\cdot}16$). The variation in the bilayer separation ($2b_w$) is independent of defect geometry.

Table 4. Geometric parameters, for samples with $\Psi \neq 0$, derived from the NMR and SAXS data assuming pore defects.

Sample	Pore separation $(2b+2c)$/Å	Pore diameter $2c_w$/Å	Aqueous layer thickness $2b_w$/Å
D1	40 ± 5	33 ± 3	35 ± 3
D2	61 ± 9	32 ± 5	41 ± 3
D3	173 ± 107	46 ± 23	47 ± 4
Wb1	34 ± 4	25 ± 3	41 ± 3
Wb2	40 ± 5	33 ± 3	35 ± 3
Wb3	42 ± 5	24 ± 3	36 ± 3
Wb4	42 ± 5	23 ± 3	30 ± 3
Wb5	44 ± 6	22 ± 4	28 ± 3
Wb6	46 ± 7	13 ± 4	28 ± 3
Wb7	53 ± 8	25 ± 5	21 ± 2
Wb8	65 ± 17	9 ± 8	18 ± 2

assume, as in § 3, that defects are introduced under the constraint of constant bilayer thickness ($b=11{\cdot}6$ Å). Since a variation in Ψ then necessarily changes the surface to volume ratio in the system, we must minimize the free energy of a fixed volume V (rather than a fixed surface area). Accordingly, we introduce a dimensionless free energy density,

$$g(\Psi)=\frac{G(\Psi)b^3}{k_BTV}, \tag{4.1}$$

defined so that $g(\Psi=0)=0$.

Any physically acceptable description of $g(\Psi)$ must feature at least two contributions; one which promotes defects and another which opposes defects [24]. It is convenient to imagine that the defects are formed in two steps. In the first step, water is transferred from the inter-bilayer space to an imagined reservoir in osmotic equilibrium with the L_α phase, thereby reducing the aqueous layer thickness from the value $2b_w^0$ that it would have in the absence of defects ($\Psi = 0$) to its actual value $2b_w$. Due to the enhanced interbilayer repulsion, this step entails a positive free energy change, which we denote $g_R(\Psi)$. In the second step, the aqueous layer thickness is held fixed at $2b_w$ while the defects are formed, and the water removed in the first step is transferred from the reservoir to the defects. The negative free energy change in this step, due to the favourable defect self-energy, is denoted $g_S(\Psi)$. Thus,

$$g(\Psi) = g_R(\Psi) + g_S()). \tag{4.2}$$

To prevent the bilayer from disintegrating, $g_R(\Psi)$ must increase faster than $-g_S(\Psi)$ for sufficiently large Ψ. If $g_R(\Psi)$ increases faster than $-g_S(\Psi)$ for all Ψ, defects will not form. If this is not the case, there may exist a stable state with $\Psi > 0$, i.e. a state with $dg/d\Psi = 0$, $d^2g/d\Psi^2 > 0$, and $g(\Psi) < g(0)$. (In principle, the driving force for defect formation could be a thickening of the bilayers, which may reduce the total interfacial free energy. However, this cannot be the case if, as argued in § 3.1, defects are formed under the constraint of constant bilayer thickness.)

In a more sophisticated treatment, one would add to equation (4.2) an entropic contribution reflecting the in-plane distribution of defects and a contribution due to defect–defect interactions. While these contributions are essential in considerations of possible phase transitions among L_α phases with different defect patterns [24], they are likely to be much smaller than the two terms in equation (4.2) and, hence, do not significantly affect the equilibrium Ψ value [24].

The scaling behaviour of the two free energy contributions in equation (4.2), i.e. their dependence on the volume fractions ϕ and Ψ, can be established without specifying the defect geometry or the physical origin of the interactions. Neglecting defect polydispersity, the self-energy density g_S scales as the three-dimensional defect density, or as the two-dimensional (in the bilayer plane) defect density divided by the lamellar period d. Since the two-dimensional defect density is proportional to the intrabilayer defect volume fraction Ψ and since $d = 2b(1-\Psi)/\phi$, it follows that [24]

$$g_S(\Psi) = -g_d \frac{\phi\Psi}{1-\Psi}. \tag{4.3}$$

The quantity g_d is the self-energy density of an individual defect (in reduced units), i.e.

$$g_d = -\frac{G_d b^3}{k_B T V_d}, \tag{4.4}$$

with G_d the (negative) self-energy for a defect of volume V_d. (This is the volume of polar material contained within a defect in the lamellar hydrocarbon core of thickness $2b$.)

The expression (4.3) is useful only to the extent that the defect volume V_d is fixed so that g_d is independent of ϕ and Ψ. On the basis of the analysis in § 3.2, yielding an essentially constant slit width or pore diameter (cf. tables 3 and 4), we assume that this is the case. The scaling relation (4.3) then applies to, for example, slit and pore defects of arbitrary (fixed) geometry, but not to water-continuous microstructures. (In the latter case, Ψ is not a proper variational parameter.)

Under the conditions of the present study (high surface charge density, no added salt, relatively large bilayer separation, the dominant contribution to $g_R(\Psi)$ is the electrostatic inter-bilayer repulsion [35]. Moreover, for all investigated samples, we are in the strong-coupling regime (the Gouy–Chapman length is 1–2 Å [23]), where this repulsion is inversely proportional to the thickness $2b_w = d - 2b$ of the inter-bilayer aqueous region accessible to the counterions, and is independent of the surface charge density [23]. It follows then that g_R scales as $(1/d)(1/b_w)$, where $1/d$ is the one-dimensional bilayer density. The explicit form of g_R becomes [23, 35]

$$g_R(\Psi) = g_e\left[\frac{\phi^2}{(1-\Psi)(1-\Psi-\phi)} - \frac{\phi^2}{(1-\phi)}\right], \tag{4.5}$$

with

$$g_e = \frac{\pi b}{8\lambda_B}. \tag{4.6}$$

With $b = 11{\cdot}6$ Å (cf. § 3.1) and the Bjerrum length $\lambda_B = 7{\cdot}14$ Å (appropriate for H_2O at 25°C), we thus have $g_e = 0{\cdot}638$.

The variational free energy density can now be expressed as

$$g(\Psi) = -g_d\frac{\phi\Psi}{1-\Psi} + g_e\left[\frac{\phi^2}{(1-\Psi)(1-\Psi-\phi)} - \frac{\phi^2}{(1-\phi)}\right], \tag{4.7}$$

which, as required, vanishes in the limit $\Psi \to 0$. This free energy density is of the same form as that used by Bagdassarian *et al.*, to describe the 'stripe phase' [24].

By differentiating equation (4.7) with respect to Ψ, we find that the bilayer can support defects ($\Psi > 0$) only if

$$K \equiv \frac{g_d}{g_e} > \frac{\phi(2-\phi)}{(1-\phi)^2}, \tag{4.8}$$

and that the equilibrium defect volume fraction Ψ decreases linearly with ϕ according to

$$\Psi = 1 - \frac{1 + K + \sqrt{(1+K)}}{K}\phi. \tag{4.9}$$

The dimensionless interaction parameter K measures the intrinsic propensity of the bilayer for supporting defects. Figure 8 shows the variational free energy function $g(\Psi)$ for $K = 1{\cdot}5$ and several volume fractions ϕ.

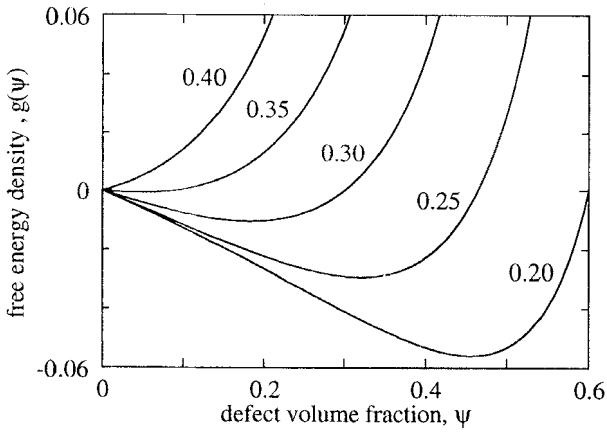

Figure 8. Reduced free energy density $g(\Psi)$ versus defect volume fraction Ψ for $K = 1{\cdot}5$ ($g_e = 0{\cdot}638$) and the indicated volume fractions ϕ. For $\phi > 0{\cdot}368$, defects will not form.

4.2. *Defect energetics*

Although the defect volume fraction Ψ obtained from the SAXS data (cf. table 2) does decrease linearly with ϕ (within experimental error), it is not described by equation (4.9). In particular, the magnitude of the slope is an order of magnitude larger for the **D** line than for the **Wb** line. Also, if the linear fits (not shown) of the (ϕ, Ψ) data are used to determine the ϕ value where $\Psi = 0$, we obtain from equation (4.8) $K = 1{\cdot}2$ for the **D** line and $K = 4{\cdot}8$ for the **Wb** line. It is clear, therefore, that the defect self-energy G_d (and, hence, K) depends on composition (x, y). To quantify this dependence, we calculate K for each sample with $\Psi > 0$, using equation (4.9) in the rearranged form

$$K = \frac{\phi(2 - 2\Psi - \phi)}{(1 - \Psi - \phi)^2}. \tag{4.10}$$

The resulting K values for the **D** and **Wb** lines, as well as for the **D** line in the system **SdS**/decanol/water [16], are given in table 2. The effect of this K variation is seen in figure 9, where we compare the defect volume fractions Ψ derived from the SAXS data with those calculated from equation (4.9) with a fixed value of $K = 1{\cdot}5$.

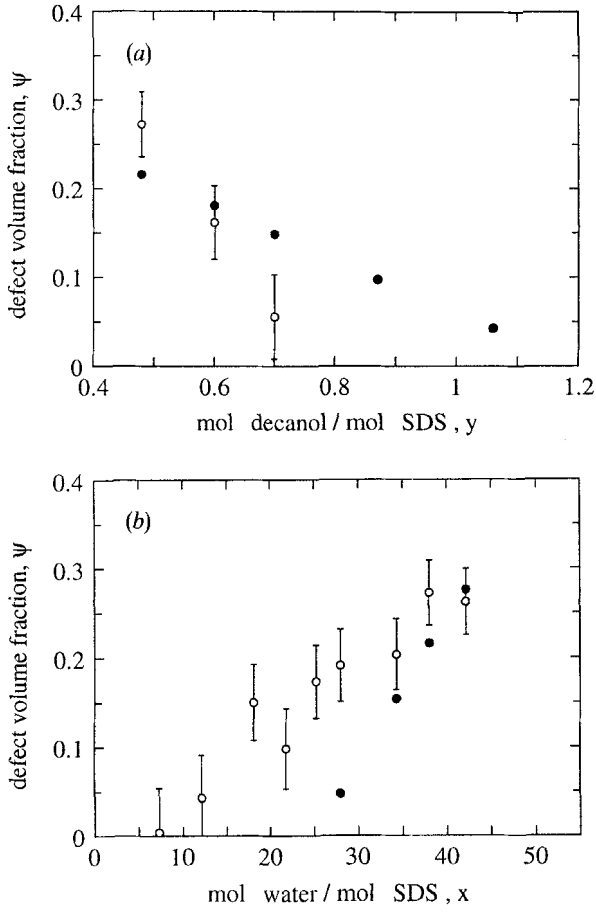

Figure 9. Variation of the defect volume fraction Ψ with composition along (*a*) the **D** line and (*b*) the **Wb** line. Open symbols correspond to the experimental Ψ values from table 2, and the solid symbols to Ψ values calculated from equation (4.9) with a fixed $K = 1{\cdot}5$.

Figure 9 (*b*) shows that, as the water content is reduced, Ψ decreases more slowly than expected from equation (4.9). Within the present formalism, this means that the defect self-energy becomes more negative (larger K; cf. table 2) as the water content is reduced. As seen from figure 9 (*a*), Ψ decreases strongly with increased decanol content (y) in the bilayer. Clearly, the strong reduction of Ψ with increasing y is essentially due to a reduced intrinsic defect propensity (less negative self-energy) with increasing decanol content, rather than to the (slight) increase in ϕ. This is not unexpected in view of the phase behaviour (cf. § 4.3).

A microscopic analysis of the self-energy of a defect, G_d, and its variation with composition, will not be attempted here. However, some insight can be gained from a simple phenomenological approach. We thus regard G_d as the sum of a positive interfacial free energy and a negative curvature free energy. The former reflects the increased hydrocarbon–water contact as defects are formed (at constant bilayer thickness), while the latter is taken to include all curvature-dependent free energy contributions, notably electrostatics and chain packing. We thus write

$$G_d = \gamma(A_C - A_P) + [\tfrac{1}{2}\kappa(c_1 + c_2 - c_0)^2 - \tfrac{1}{2}\kappa c_0^2]A_C, \tag{4.11}$$

with γ the effective interfacial tension [25, 36–38], κ the bending (splay) elastic modulus, c_1 and c_2 the principal curvatures, c_0 the spontaneous curvature [39, 40], A_C the area of the curved region, and A_P the planar area of the same volume of bilayer. For simplicity, we consider only the slit/ribbon geometry, where the curvatures are uniform ($c_1 = 1/b$, $c_2 = 0$). Straightforward geometric considerations then yield with equations (4.4), (4.8), and (4.11),

$$K = \frac{\kappa(2c_0 b - 1) - \gamma b^2}{[(4/\pi)\zeta - 1]g_e k_B T} \approx 623(\gamma_C - \gamma), \tag{4.12}$$

where we have inserted numerical values ($g_e = 0{\cdot}638$, $b = 11{\cdot}6$ Å, $\zeta = 1 + c_w/b = 1 + 5/11{\cdot}6$) and defined

$$\gamma_C = \frac{\kappa}{b^2}(2c_0 b - 1). \tag{4.13}$$

With $\gamma = 18{\cdot}0$ mJ m^{-2} [25, 36–38], we thus need $\gamma_C = 20{\cdot}4$ mJ m^{-2} to get a typical value of $K = 1{\cdot}5$ (cf. table 2). The near cancellation of the two contributions illustrates the difficulty that would be encountered in a microscopic calculation of the defect self-energy. With a reasonable value of $\kappa \approx 10 k_B T$ [23, 41], equation (4.13) yields a spontaneous curvature of $c_0 \approx (14\text{ Å})^{-1}$. This thermodynamic quantity may be related to the (spherical) equilibrium curvature c_{eq}, which minimizes the curvature free energy [40, 42] through $c_0 = (2 + \kappa/\kappa)\, c_{eq}$, with $\bar{\kappa}$ the gaussian (saddle-splay) elasticity modulus. If $|\bar{\kappa}| \ll \kappa$, we thus arrive at $c_{eq} \approx (28\text{ Å})^{-1}$. This value is not unreasonable in view of the nearby presence in the phase diagram of nematic and hexagonal phases (cf. figure 1).

The deduced variations of K (table 2) may be qualitatively interpreted in terms of variations of the parameters in equation (4.12). Since the defect geometry appears to be fixed (§ 3.2), the variables are κ, c_0, and γ. The reduction of K with increasing decanol content along the **D** line probably reflects a reduction of the spontaneous curvature as the mean head group area per amphiphile decreases [43]. The effect of decanol addition on (the chain packing contribution to) κ is likely to be smaller [44]. The reported decrease of γ with decanol addition [36, 38] obviously cannot explain a reduction of K; this effect is either overshadowed by a stronger c_0 variation or is an artifact of the neglect of defects (cf. Appendix). The larger K values for the **SdS** system can be largely ascribed to the higher volume fraction ($\phi \approx 0{\cdot}44$ versus $\approx 0{\cdot}30$), an effect also seen along the **Wb** line. The origin of this effect probably lies in the electrostatic interactions.

To obtain more information on the thermodynamics of defect formation, we have measured the temperature dependence of the quadrupole splitting ν_Q in the range 20–40°C. As seen from table 5, ν_Q is nearly independent of temperature. This tempertuare independence carries over to the shape factor, since the residual quadrupole coupling $\bar{\chi}$ is known not to vary significantly with temperature in this range [28–30, 45, 46]. If the defect dimensions (b and c_w) do not change, this implies that Ψ and, hence, K are nearly independent of temperature. This appears surprising in view of the delicate balance of the two opposing contributions to K. (The numerical factor in equation (4.12) decreases by 4 per cent as the temperature is raised from 20 to 40°C.)

4.3. *Defects and phase behaviour*

It is clear that defect formation in the L_α phase is governed by the same factors that determine the relative stability of the L_α phase with respect to neighbouring phases. A glance at the phase diagram in figure 1 reveals the crucial importance of the decanol/**SDS** ratio (y) in determining the phase boundaries and the relative insensitivity of the phase boundaries to water dilution (at constant y). With decreasing decanol content, there is a progression towards phases with more highly curved interfaces: $L_\alpha \rightarrow N_D \rightarrow N_C \rightarrow H_\alpha \rightarrow$isotropic micellar. The appearance of curvature defects in the L_α phase with decreasing y fits nicely into this progression.

Table 5. Temperature dependence of the ^2H quadrupole splitting ν_Q.

	ν_Q/kHz†		
Sample	20°C	30°C	40°C
D1	17·7	16·6	‡
D2	21·6	20·4	‡
D3	24·4	23·3	23·4
D4	25·2	24·2	23·6
D5	25·2	24·4	23·9
D6	25·5	24·5	23·9
D7	25·3	24·5	23·8
D8	25·3	24·3	23·6
Wa1	24·8	24·1	23·5
Wa2	25·2	24·4	23·9
Wa3	25·2	24·4	23·9
Wa4	25·4	24·8	24·4
Wa5	26·3	25·8	25·6
Wb1	16·3	‡	‡
Wb2	17·7	16·6	‡
Wb3	18·7	17·7	‡
Wb4	19·0	18·2	17·5
Wb5	19·5	18·8	18·2
Wb6	20·6	20·2	19·7
Wb7	20·7	20·7	20·7
Wb8	23·0	23·4	23·7
Wb9	26·3	26·0	25·8

† Uncertainty: ±0·2 kHz.
‡ Sample in two phase region.

Within a phenomenological description, one would say that curvature defects within the L_α phase and transitions to phases with more highly curved microstructures are both driven by an increase in spontaneous curvature. Defect formation provides a mechanism to relieve the frustration associated with a large spontaneous curvature in the L_α phase [47], and may be viewed as a pretransitional effect, heralding the approach to the (first order) $L_\alpha \rightarrow N_D$ phase transition. The defect volume fraction Ψ increases as the transition is approached by reducing the decanol content (**D** line) and also (but much less strongly) when it is approached by increasing the temperature (cf. table 5). It is also noteworthy that the onset of defects occurs at the same decanol/surfactant ratio ($y \approx 0{\cdot}8$) in the **SDS** and **SdS** systems, despite considerable differences in the phase diagrams.

In the slit defect model, the microstructure of the defective L_α phase is closely related to the rectangular (R_α) or ribbon phases [34, 48–52]. Indeed, in the L_α samples with the highest defect volume fraction, the aspect ratio of the ribbon cross-section is about 2 (cf. table 3 and figure 7), which is only slightly larger than the values 1·3–1·9 reported for R_α phases [34]. The main difference between these phases is that the ribbons in the R_α phase are translationally ordered in two dimensions, while the ribbons in the L_α phase are ordered in only one dimension, although there may be short range positional correlations between the layers [16, 17]. It is noteworthy that the L_α phase in the **SdS** system studied by Hendrikx *et al.* [16], transforms into an R_α phase along their **D** line, whereas no R_α phase has yet been found in the corresponding region of the phase diagram of the **SDS** system.

In their theoretical study, Bagdassarian *et al.* [24], consider several phases distinguished by different in-plane defect patterns, but all having the macroscopic $D_{\infty h}$ symmetry of an L_α phase. A distinct defective L_α phase, separated from the normal L_α phase by a first order transition, has recently been reported for the non-ionic system $C_{22}EO_6$/water [22]. For the present system, however, there is no sign of a first order transition between different L_α phases. Although the abrupt onset of defects at $y \approx 0{\cdot}8$ could be interpreted as a second order transition, the gradual disappearance of these defects along the **Wb** line argues against this possibility.

5. Conclusions

We have presented the results of a combined NMR and SAXS study of structural defects in the L_α phase of the system **SDS**/decanol/water. In particular, we have focused on the variation of the density and size of the defects with composition ($0{\cdot}27 < \phi < 0{\cdot}64$, $0{\cdot}46 < y < 2{\cdot}54$) and temperature (20–40°C). The main conclusions are as follows.

(1) Bilayer defects are promoted by the same factors that drive the phase progression towards microstructures with increasingly curved interfaces, i.e., the defect volume fraction increases on dilution of the L_α phase and on decreasing the decanol content of the bilayers.

(2) No defects are found above 0·8 mol decanol/mol **SDS**; below this value the defect volume fraction increases rapidly. At decanol contents where defects occur, the defect volume fraction decreases gradually as the L_α phase is concentrated and disappear completely near the high-ϕ boundary of the L_α phase.

(3) Irrespective of whether the bilayer composition or the bilayer volume fraction is changed, it is the number of defects that varies rather than their size.

(4) Temperature variations within the range of stability of the L_α phase have little effect on the defect volume fraction.

(5) Our data do not allow the defect geometry to be uniquely determined. The data are consistent with slit defects (slit width *c.* 10 Å) as well as with pore defects (pore diameter *c.* 25 Å). In both cases, the (average) interface separation across the defect is considerably smaller than across the inter-lamellar space.

(6) We find no evidence of (first or second order) transitions between classical and defective L_α phases or between L_α phases with different defect patterns. On the other hand, we cannot rule out a continuous variation of defect geometry, for example, from slit defects at high Ψ to pore defects at low Ψ [24].

(7) A simple thermodynamic model, featuring a constant self-energy per defect and an electrostatic bilayer repulsion, does not quantitatively account for the data. As the L_α phase is concentrated, the defects disappear more slowly than expected from an increased inter-bilayer repulsion with a constant self-energy. The variation in the defect volume fraction with the decanol/**SDS** ratio is essentially due to a variation in the defect self-energy. The self-energy appears to be the result of a delicate balance between an interfacial free energy, which opposes defects, and electrostatic and curvature contributions, which promote defects.

We are grateful to Dr Bengt Jönsson for helpful discussions, to Dr Lars Bengtsson for assistance with the Varian spectrometer, and to the Swedish Research Council for Engineering Sciences and the Swedish Natural Science Research Council for financial support.

Appendix. Calculation of optimal bilayer thickness

Following Parsegian [25], we estimate the bilayer thickness $2b$ in a classical (defect-free) L_α phase by minimization of the free energy $G(b)$ with respect to variations in b at fixed volume fraction ϕ. It is convenient to consider the reduced (by k_BT) free energy per (average) amphiphile,

$$g(b)=\frac{G(b)v_m}{k_BTV\phi}, \tag{A 1}$$

with

$$v_m=\frac{v_{SDS}+yv_{dec}}{1+y}. \tag{A 2}$$

We assume that $g(b)$ consists of two parts,

$$g(b)=g_e(b)+g_i(b). \tag{A 3}$$

The electrostatic free energy, $g_e(b)$, tends to make the bilayer thinner, thereby reducing the surface charge density at the hydrocarbon–water interface. The interfacial free energy, $g_i(b)$, tends to thicken the bilayer, thereby reducing the interface area. Since variations in b take place under the constraint of fixed volume fraction ϕ, the electrostatic term pushes the charged surfaces together, while the interfacial term drives them apart.

Within the usual mean-field (Poisson–Boltzmann) approximation, the electrostatic free energy takes the form [25]

$$g_e(b)=\frac{1}{1+y}\left[\ln\left(\frac{2q}{\sin 2q}\right)-1+\frac{q}{\tan q}\right]. \tag{A 4}$$

The b dependence enters via the dimensionless parameter q, which is obtained by solving the transcendental equation

$$q \tan q = \frac{2\pi\lambda_B(1-\phi)}{(1+y)v_m\phi} b^2. \tag{A 5}$$

The phenomenological interfacial free energy is (to within an irrelevant constant)

$$g_i(b) = \frac{v_m\gamma}{k_B T}\frac{1}{b}, \tag{A 6}$$

where γ is an effective interfacial tension [25, 36–38]. Apart from the hydrophobic free energy of the residual hydrocarbon–water contact, γ also accounts for the conformational free energy of the hydrocarbon chains, the entropy of mixing of the head groups, and the deficiencies in the description of the electrostatic contribution. By comparing the observed lamellar period d with that predicted ($d = 2b/\phi$) by minimizing (A 3) with respect to b under conditions where $b < b_{max}$ and where there are no defects, one can determine γ. Remarkably, an essentially invariant value of $\gamma \approx 18{\cdot}0\,\mathrm{mJ\,m^{-2}}$ is obtained for a range of binary systems [25, 36–38]. A similar value ($18{\cdot}5\,\mathrm{mJ\,m^{-2}}$) was obtained by comparing calculated and experimental aggregation numbers of **SDS** micelles [53].

Figure 10 shows the variation of the free energy $g(b)$, as given by (A 3)–(A 6), with the bilayer thickness for a composition corresponding to sample **D1**. The minimum in $g(b)$ occurs at $b = 11{\cdot}7$ Å. The variation of the equilibrium bilayer thickness with composition along the **D** and **Wb** lines is shown in figure 11. (Along the **Wa** line, **b** varies between 15·6 and 17·7 Å.) As seen from figure 11, $b > b_{max} = 11{\cdot}6$ Å (cf. § 3.1) for all investigated samples. Hence, the actual bilayer thickness is not determined by the balance between the inter-bilayer electrostatic and interfacial free energies, but rather by the short-ranged lateral repulsion between surfactant headgroups, yielding $b = b_{max} = 11{\cdot}6$ Å for all investigated samples.

In all these calculations, we have used a fixed value of $\gamma = 18\,\mathrm{mJ\,m^{-2}}$. A previous analysis of SAXS data from L_α phases in ternary systems containing decanol or octanol suggests that γ should decrease with y [36, 38]. However, this conclusion relies on the

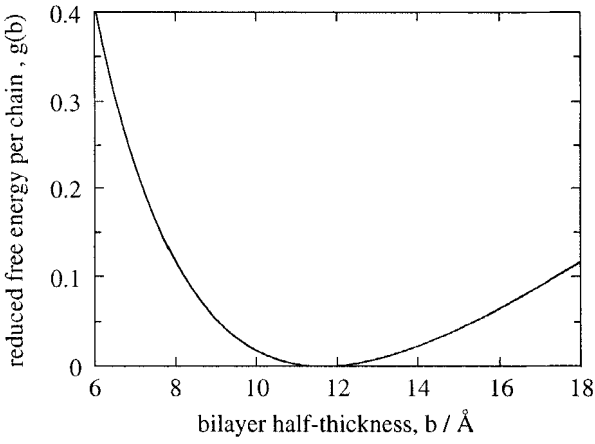

Figure 10. Reduced free energy per chain $g(b)$ versus bilayer half-thickness b for sample **D1** ($x = 38$, $y = 0{\cdot}48$, $\gamma = 18\,\mathrm{mJ\,m^{-2}}$).

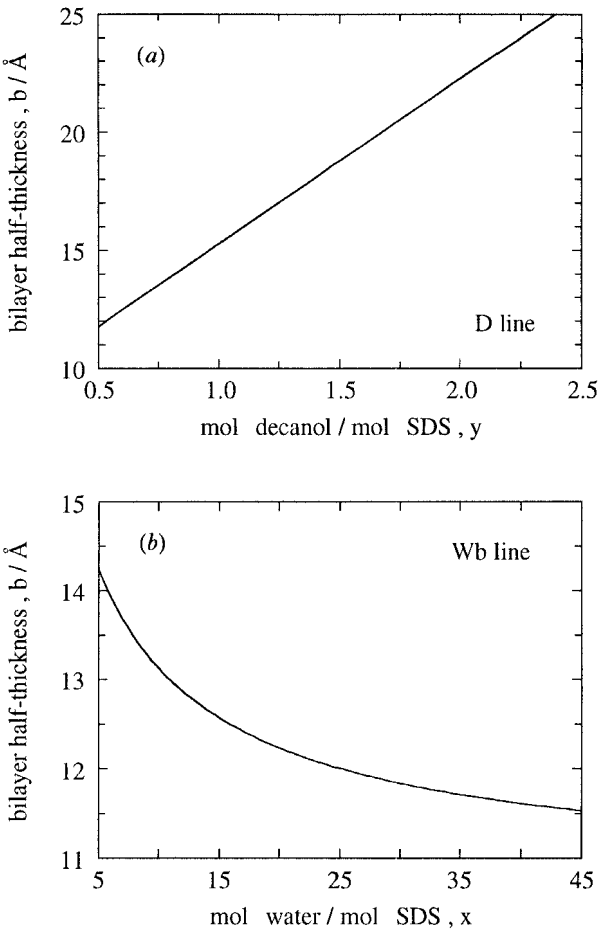

Figure 11. Variation of the equilibrium bilayer half-thickness b with composition along (*a*) the **D** line ($x = 38{\cdot}2$), and (*b*) the **Wb** line ($y = 0{\cdot}48$).

assumption of a defect-free microstructure. It is possible that the apparent increase of γ with decreasing decanol content is instead due to an increasing defect volume fraction Ψ, which reduces the apparent bilayer thickness ϕd (cf. § 3.1). To explain the value $\phi d = 16{\cdot}9$ Å, observed for sample **D1** in the present system, by bilayer thinning alone, we would need $\gamma = 12\,\mathrm{mJ\,m^{-2}}$.

References

[1] TIDDY, G. J. T., HAYTER, J. B., HECHT, A. M., and WHITE, J. W., 1974, *Ber. Bunsenges. phys. Chem.*, **78,** 961.
[2] TIDDY, G. J. T., 1977, *J. chem. Soc. Faraday Trans. I*, **73,** 1731.
[3] GAULT, J. D., KAVANAGH, E., RODRIGUES, L. A., and GALLARDO, H., 1986, *J. phys. Chem.*, **90,** 1860.
[4] CHIDICHIMO, G., COPPOLA, L., LA MESA, C., RANIERI, G. A., and SAUPE, A., 1988, *Chem. Phys. Lett.*, **145,** 85.
[5] UKLEJA, P., CHIDICHIMO, G., and PHOTINOS, P., 1991, *Liq. Crystals*, **9,** 359.
[6] PHOTINOS, P. J., YU, L. J., and SAUPE, A., 1981, *Molec. Crystals liq. Crystals*, **67,** 277.
[7] BODEN, N., CORNE, S. A., and JOLLEY, K. W., 1984, *Chem. Phys. Lett.*, **105,** 99.

[8] PHOTINOS, P., and SAUPE, A., 1986, *J. chem. Phys.*, **84,** 517.
[9] PHOTINOS, P., and SAUPE, A., 1991, *Phys. Rev.* A, **43,** 2890.
[10] BODEN, N., CLEMENTS, J., DAWSON, K. A., JOLLEY, K. W., and PARKER, D., 1991, *Phys. Rev. Lett.*, **66,** 2883.
[11] BODEN, N., and JOLLEY, K. W., 1992, *Phys. Rev.* A, **45,** 8751.
[12] HOLMES, M. C., and CHARVOLIN, J., 1984, *J. phys. Chem.*, **88,** 810.
[13] KÉKICHEFF, P., CABANE, B., and RAWISO, M., 1984, *J. Phys. Lett., Paris,* **45,** 813.
[14] BODEN, N., CORNE, S. A., HOLMES, M. C., JACKSON, P. H., PARKER, D., and JOLLEY, K. W., 1986, *J. Phys., Paris,* **47,** 2135.
[15] HOLMES, M. C., REYNOLDS, D. J., and BODEN, N., 1987, *J. phys. Chem.*, **91,** 5257.
[16] HENDRIKX, Y., CHARVOLIN, J., KÉKICHEFF, P., and ROTH, M., 1987, *Liq. Crystals,* **2,** 677.
[17] KÉKICHEFF, P., and CABANE, B., 1988, *Acta crystallogr.* B, **44,** 395.
[18] HOLMES, M. C., CHARVOLIN, J., and REYNOLDS, D. J., 1988, *Liq. Crystals,* **3,** 1147.
[19] KÉKICHEFF, P., and TIDDY, G. J. T., 1989, *J. phys. Chem.*, **93,** 2520.
[20] BODEN, N., CLEMENTS, J., JOLLEY, K. W., PARKER, D., and SMITH, M. H., 1990, *J. chem. Phys.*, **93,** 9096.
[21] LEAVER, M. S., and HOLMES, M. C., 1993, *J. Phys. II,* Paris, **3,** 105.
[22] FUNARI, S. S., HOLMES, M. C., and TIDDY, G. J. T., 1993, *J. phys. Chem.* (in the press).
[23] QUIST, P-O., and HALLE, B., 1993, *Phys. Rev.* E, **47,** 3374.
[24] BAGDASSARIAN, C. K., ROUX, D., BEN-SHAUL, A., and GELBART, W. M., 1991, *J. chem. Phys.*, **94,** 3030.
[25] PARSEGIAN, V. A., 1966, *Trans. Faraday Soc.*, **62,** 848.
[26] CHARVOLIN, J., and HENDRIKX, Y., 1985, *Nuclear Magnetic Resonance of Liquid Crystals,* edited by J. W. Emsley (D. Reidel Publ. Co.), p. 449.
[27] KLASON, T., and HENDRIKSSON, U., 1982, *Solution Behavior of Surfactants,* Vol. 1, edited by K. L. Mittal and E. J. Fendler (Plenum Press), p. 417.
[28] ABDOLALL, K., MACKAY, A. L., and BLOOM, M., 1978, *J. magn. Reson.*, **29,** 309.
[29] QUIST, P-O., HALLE, B., and FURÓ, I., 1991, *J. chem. Phys.*, **95,** 6945.
[30] MELY, B., CHARVOLIN, J., and KELLER, P., 1975, *Chem. Phys. Lipids,* **15,** 161.
[31] MELY, B., and CHARVOLIN, J., 1977, *Chem. Phys. Lipids,* **19,** 43.
[32] HALLE, B., LANDGREN, M., and JÖNSSON, B., 1988, *J. Phys.* Paris, **49,** 1235.
[33] ALPÉRINE, S., HENDRIKX, Y., and CHARVOLIN, J., 1985, *J. Phys. Lett., Paris,* **46,** 27.
[34] HAGSLÄTT, H., SÖDERMAN, O., and JÖNSSON, B., 1992, *Liq. Crystals,* **12,** 667, and references therein.
[35] COWLEY, A. C., FULLER, N. L., RAND, R. P., and PARSEGIAN, V. A., 1978, *Biochemistry,* **17,** 3163.
[36] JÖNSSON, B., 1981, Thesis, University of Lund.
[37] JÖNSSON, B., and WENNERSTRÖM, H., 1981, *J. Coll. Interface Sci.*, **80,** 482.
[38] JÖNSSON, B., and WENNERSTRÖM, H., 1987, *J. phys. Chem.*, **91,** 338.
[39] HELFRICH, W., 1973, *Z. Naturf.* (*c*), **28,** 693.
[40] HELFRICH, W., 1981, *Physics of Defects,* edited by R. Balian, M. Kléman and J. P. Poirer (North-Holland), p. 715.
[41] SAFINYA, C. R., SIROTA, E. B., ROUX, D., and SMITH, G. S., 1989, *Phys. Rev. Lett.*, **62,** 1134.
[42] FOGDEN, A., HYDE, S. T., and LUNDBERG, G., 1991, *J. chem. Soc. Faraday Trans.*, **87,** 949.
[43] ENNIS, J., 1992, *J.. chem. Phys.*, **97,** 663.
[44] SZLEIFER, I., KRAMER, D., BEN-SHAUL, A., GELBART, W. M., and SAFRAN, S. A., 1990, *J. chem. Phys.*, **92,** 6800.
[45] JEFFREY, K. R., WONG, T. C., and TULLOCH, A. P., 1984, *Molec. Phys.*, **52,** 289.
[46] DELIKATNY, E. J., and BURNELL, E. E., 1989, *Molec. Phys.*, **67,** 757.
[47] CHARVOLIN, J., 1990, *Contemp. Phys.*, **31,** 1.
[48] LUZZATI, V., MUSTACCHI, H., SKOULIOS, A., and HUSSON, F., 1960, *Acta crystallogr.*, **13,** 660.
[49] HUSSON, F., MUSTACCHI, H., and LUZZATI, V., 1960, *Acta crystallogr.*, **13,** 668.
[50] HENDRIKX, Y., and CHARVOLIN, J., 1981, *J. Phys.*, **42,** 1427.
[51] HENDRIKX, Y., and CHARVOLIN, J., 1987, *Liq. Crystals,* **3,** 265.
[52] CHIDICHIMO, G., GOLEMME, A., and DOANE, J. W., 1985, *J. phys. Chem.*, **82,** 4369.
[53] EVANS, D. F., MITCHELLL, D. J., and NINHAM, B. W., 1984, *J. phys. Chem.*, **88,** 6344.